Single-Electron Transistor Research

Personnel
D. Berman
(R. C. Ashoori and H. I. Smith)

Sponsorship
JSEP

The Single Electron Transistor (SET) has the highest charge sensitivity of any man-made device. In many respects, it is the electric analog of the SQUID, which is the most sensitive detector of magnetic field. It is very well suited for applications where one needs to measure small fluctuations of charge without disturbing the system under study. An example of such a system is a quantum dot.

Figure 1 shows a scanning-electron micrograph of one of our devices. The SET consists of a metal island connected to the source and drain electrodes by two small tunnel junctions. Fabrication of the tunnel junctions is performed using a shadow evaporation method.

The operation of the Single Electron Transistor depends on the fact that the central island has a very small capacitance and the energy that it takes for electrons to charge this island is quite large. For example, if the device is cooled to temperatures below 1K, the electron thermal energy becomes less than the charging energy. This means that without a significant source-drain voltage bias, the electrons cannot travel through the central island. This effect is known as the Coulomb blockade. The Coulomb Blockade is manifested as a zero current region in the current-voltage dependence of the SET. This effect is shown in Figure 2. The addition of gate voltage can alter the size of the Coulomb Blockade region, thus we can use this device as a transistor.

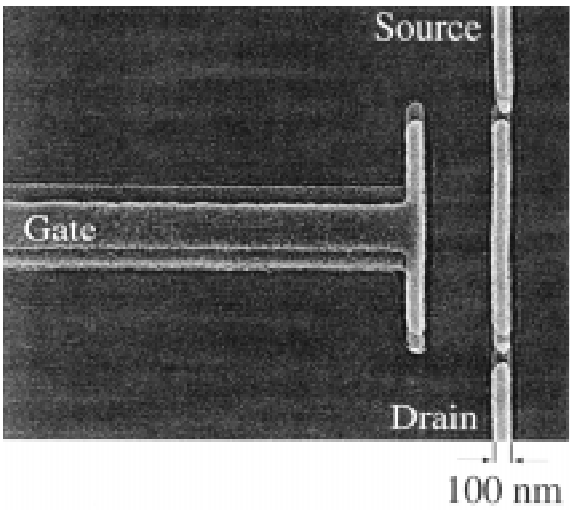

Fig. 1: Scanning electron micrograph of a single-electron transistor, made of Al, in which the two tunnel barriers are produced by a two-angle shadow evaporation process.

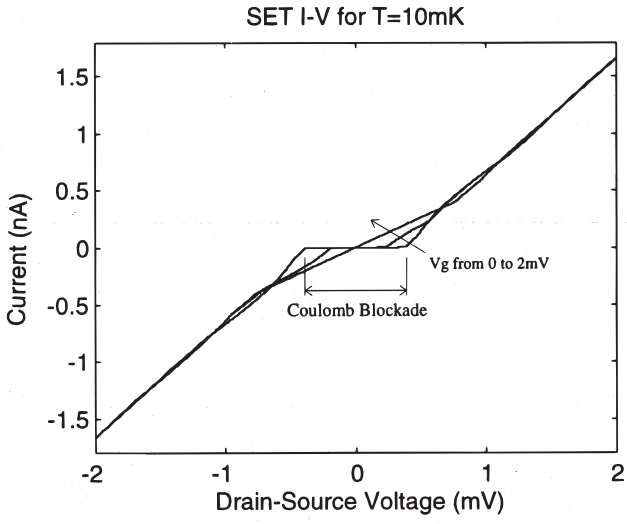

Fig. 2: Current-voltage characteristic of a single-electron transistor taken at 10 mK, for three values of gate voltage. The Coulomb blockade is maximum at zero gate bias.

continued

We have incorporated our technique of fabricating SETs into experiments with quantum dots in GaAs. Figure 3 is a micrograph of the device. The quantum dot is created in the 2DEG below the surface by applying a negative voltage to the metal leads on the surface, thereby depleting the electrons below. The SET is integrated into the lead pattern defining the quantum dot and is used to detect any electrostatic changes in the dot. In one of the experiments performed we tested the effect of point contact resistance on the Coulomb Blockade in the quantum dot. Figure 4 shows a sample of the data from this experiment. One of the point contacts to the quantum dot is completely pinched off so there is no conduction through it. The other point contact is slowly closed as one of the gates is scanned. The onset of Coulomb Blockade occurs when the point contact resistance is approximately 15 kohms. ❑

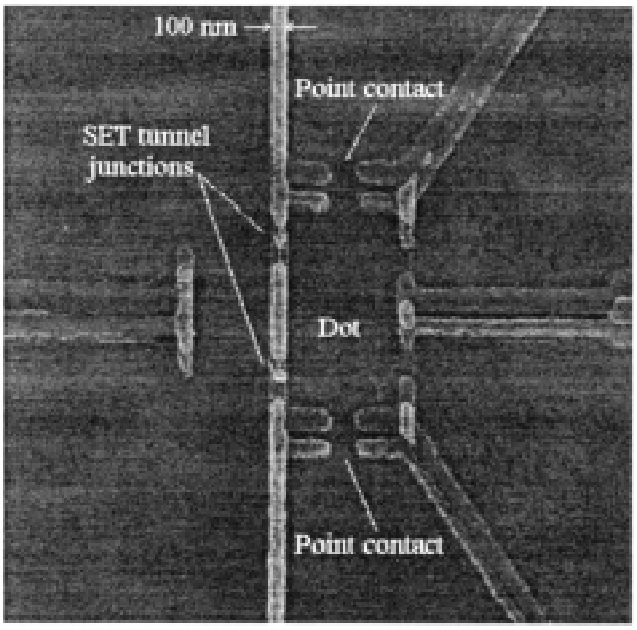

Fig. 3: Scanning-electron micrograph of a lateral quantum dot experiment. The quantum dot is defined electrostatically in the two-dimensional electron gas below the surface by applying negative voltage to the metal leads on top. The single-electron transistor is fabricated in the lead pattern, such that the central island is located next to the quantum dot for good electrostatic coupling.

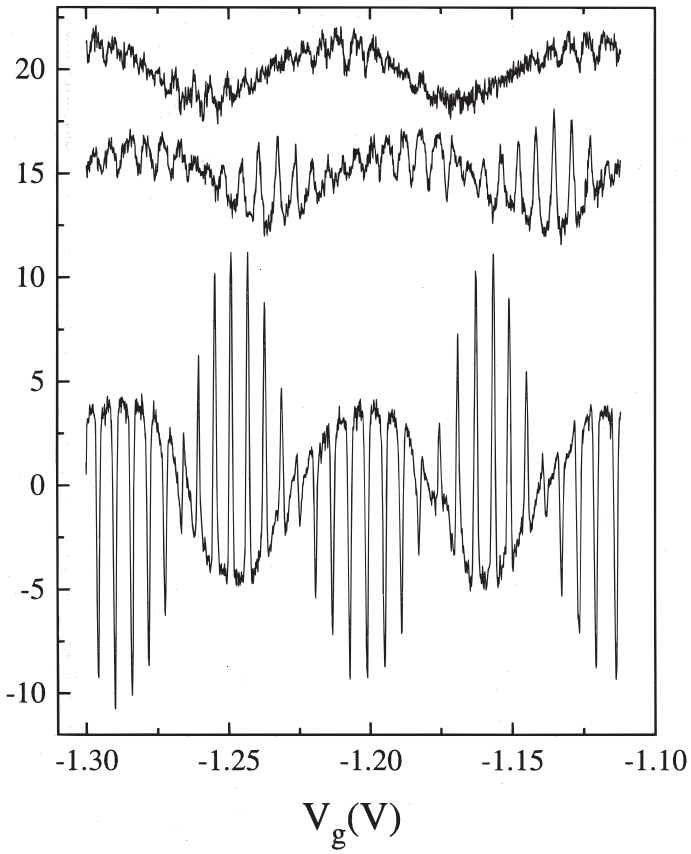

Fig. 4: The signal from the single-electron transistor as the gate of the quantum dot is varied. One of the point contacts is completely pinched off, and the resistance of the other is slowly increased from the top trace to the bottom one. The point contact resistance is increased from about 12 kohms (top trace) to 100 kohms (bottom trace). The quantization of charge, or the appearance of single-electron peaks in the signal, appears for a point contact resistance of about 15 kohms.

Electrically Pumped THz Emitters using Quantum Wells

Personnel

B. Xu
(Q. Hu in collaboration with Professor M. Melloch - Purdue University)

Sponsorship

US Army Research Office

Semiconductor quantum wells are human-made quantum mechanical systems in which the energy levels can be designed and engineered to be of any value. Consequently, unipolar lasers based on intersubband transitions (electrons that make lasing transitions between subband levels within the conduction band) were proposed for long-wavelength sources as early as the 1970s. However, because of the great challenge in epitaxial material growth and the unfavorable fast nonradiative relaxation rate, unipolar intersubband-transition lasers (also called quantum-cascade lasers) at near-infrared (4 - 5 μm) and mid-infrared (8 - 11 μm) wavelengths were developed only recently at Bell Laboratories. This achievement is remarkable, but the technique used in the original quantum-cascade lasers will not be directly applicable for the longer-wavelength THz range because of two major obstacles. First, the energy levels corresponding to THz frequencies (1 THz = 4 meV) are quite narrow, so the requirements for the design and fabrication of suitable quantum wells are demanding. Because of the narrow separation between subband levels, heating and hot-electron tunneling will have a much greater effect. Also, the small energy scales of THz photons make the detection and analysis of spontaneous emission (a crucial step toward developing lasers) quite difficult. Second and perhaps the most important, mode confinement, which is essential for any laser oscillation, is difficult at longer wavelengths. Conventional dielectric-waveguide confinement is not applicable because the evanescent field penetration, which is proportional to the wavelength and is on the order of several tens of microns, is much greater than the active gain medium of several microns. We are currently developing intersubband-transition lasers based on our recent success in generating and detecting THz emission signals and on a novel mode confinement method using metallic waveguide structures.

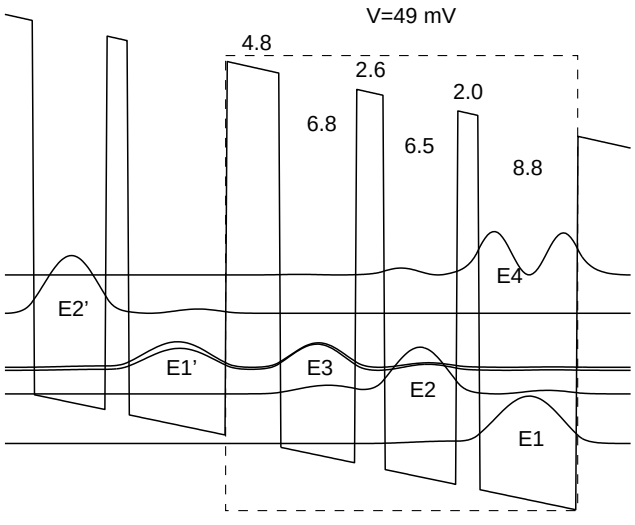

Fig. 5: Schematic of a three-level system based on a triple quantum-well structure. The radiation transition takes place between E_3 and E_2, and the fast LO-phonon emission keeps the level E_2 empty. The conduction-band profile and the square of the electron wavefunctions were calculated numerically from Schrödinger and Poisson equations.

Our MQW structure for THz emission is shown in Figure 5, in which the conduction band profile and the square of the wave functions were calculated self-consistently from Schrödinger and Poisson equations. The device is formed by a triple-well structure using $GaAs/Al_{0.3}Ga_{0.7}As$ materials, as shown in the dashed box. This structure is essentially a three-level system (marked as E_3, E_2, and E_1 in Figure 5; the level E_4 is much higher in energy so it does not contribute to transport at low biases), which is required for any lasers. Because there is no recombination involved in unipolar intersubband lasers, electrons can be "reused" many times. Consequently, many identical triple-well modules can be cascade-connected, and the emission power and the mode confinement factor can be increased substantially. Due to translational symmetry, design analysis needs to focus only on one module, provided there are no global space charges and high-field domains. The collector barrier (the one with a 2.0-nm

continued

continued

thickness) is center δ-doped at approximately $10^{11}/cm^2$ in order to provide dynamic charges to assure a global charge neutrality. The radiative transition takes place between E_3 and E_2, with an energy separation of $\Delta E_{32} \approx$ 14 meV and an oscillator strength of $f_{32} \approx 0.31$ (using the effective mass in GaAs). Under the designed bias of 50 mV per module, the ground state E_1' of a previous module is aligned with E_3. Thus, the upper subband E_3 can be selectively populated through resonant tunneling. The energy separation between E_2 and E_1 was designed to be 36 meV under the bias, which corresponds to the LO-phonon energy $\acute{O}\omega_{LO}$ in GaAs. Once energetically allowed, the very fast LO-phonon scattering (with a time $\tau_{21} \approx 1.4$ ps) will rapidly depopulate the E_2 level and establish a population inversion between E_3 and E_2.

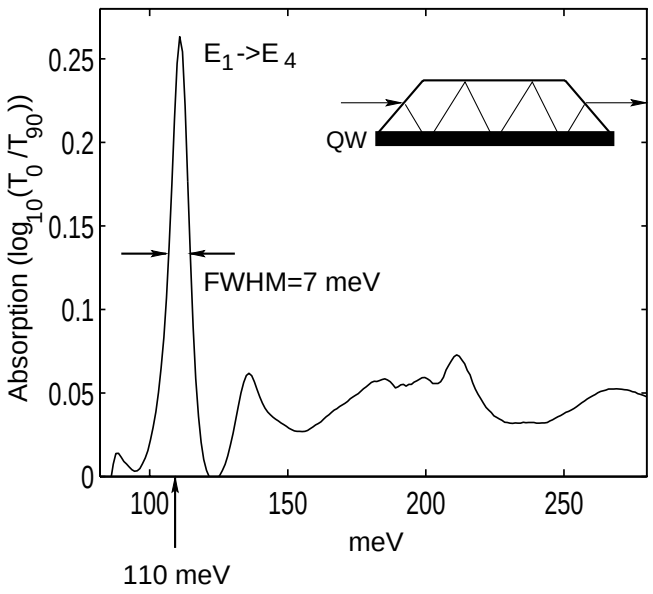

Fig. 6: Infrared absorption measurement of a 80-module device, which was placed at room temperature. The absorption peak is due to the $E_1 \rightarrow E_4$ intersubband transition. The measured FWHM is 7 meV, including a 4-meV instrumental linewidth. The measured intersubband transition frequency (110 meV) and dipole moment (14 A) agreed quite well with the calculated values of 109 meV and 12 A.

The MQW structures were grown in the Molecular-Beam Epitaxy (MBE) machine in the group of our collaborator Professor M. R. Melloch at Purdue University. In order to verify the accuracy of our design calculations and to inspect the quality of quantum wells and interfaces, we performed an infrared absorption measurement with the result shown in Figure 6. The measurement was performed on a 80-module device (with a total of 240 quantum wells) at room temperature. A mid-infrared absorption peak is clearly seen at 110 meV, which is due to the intersubband transition from E_1 to E_4. The FWHM is only 7 meV, including a 4-meV instrumental linewidth. This narrow linewidth is an indication of the high quality and uniformity of the wells and interfaces. Furthermore, the measured $E_1 \rightarrow E_4$ transition frequency of 110 meV and the dipole moment of 14 Å (deduced from the area of the absorption peak) agreed quite well with the calculated values of 109 meV and 12 Å, indicating the accuracy of our calculations.

In order to measure the intersubband THz emission and resolve its spectra, we constructed a set-up that included an external Fourier Transform InfraRed spectrometer (FTIR) with a composite Si bolometer as its detector. The system's schematic is shown in Figure 7. We have improved this system and perfected our measurement techniques so that THz emission measurements can be routinely performed on our emitters with output power levels of 1-10 nW.

Using the emission measurement system shown in Figure 7, we resolved the emission spectra from many different MQW devices and at different biases. A representative one is shown in Figure 8. This result was obtained from a 10-module device using a metallic grating with a period of 10 micron for surface emission. At a bias of 0.55 V, which is slightly higher than the designed value (0.5 V for 10 modules), the emission spectrum exhibits two peaks at 26 meV and 40 meV. The FWHM for both peaks is approximately 5 meV

continued

(including a 4-meV instrumental linewidth). According to our simulation, the lower emission peak is due to the $E_3 \rightarrow E_2$ transition, and the higher one is due to the $E_2 \rightarrow E_1$ transition. One important conclusion that can be drawn from this spectrum is the relative subband populations. Similar to the absorption measurement discussed earlier, the area of an emission peak is proportional to the product of the oscillator strength and the upper-level electron population. Our calculation indicated that the two transitions $E_3 \rightarrow E_2$ and $E_2 \rightarrow E_1$ have comparable oscillator strengths ($f_{32} = 0.31$ and $f_{21} = 0.27$). In Figure 7, the area of the $E_3 \rightarrow E_2$ peak is approximately twice that of the $E_2 \rightarrow E_1$ peak, thus yielding an inverted population condition $n_3 \approx 2n_2$. We believe this to be the first observation of inverted populations in electrically pumped intersubband THz emitters, and is a promising indication of the feasibility of THz lasers based on intersubband transitions. ❑

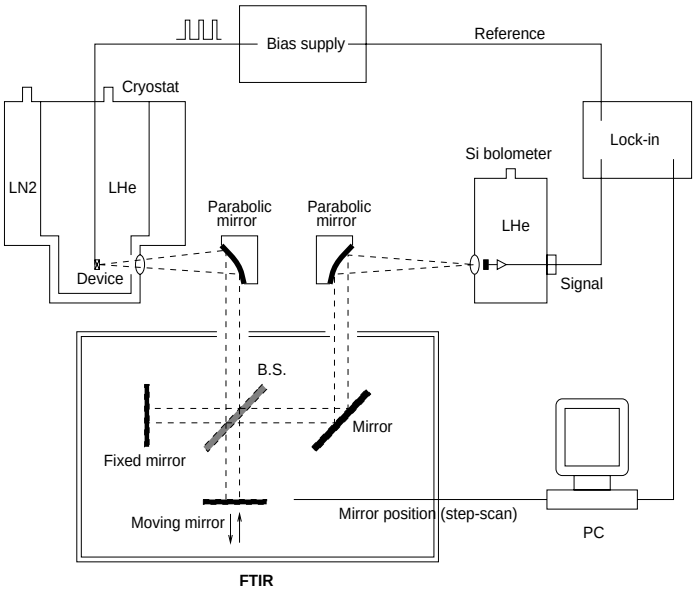

Fig. 7: (Right) THz emission spectrum from a 10-module device. The device is submerged in liquid helium and the total bias is 0.55 V. The lower emission peak at 26 meV is attributed to the $E_3 \rightarrow E_2$ transition, and the higher peak at 40 meV is due to the $E_2 \rightarrow E_1$ transition. The FWHM of both peaks is approximately 5 meV including a 4-meV instrumental linewidth.

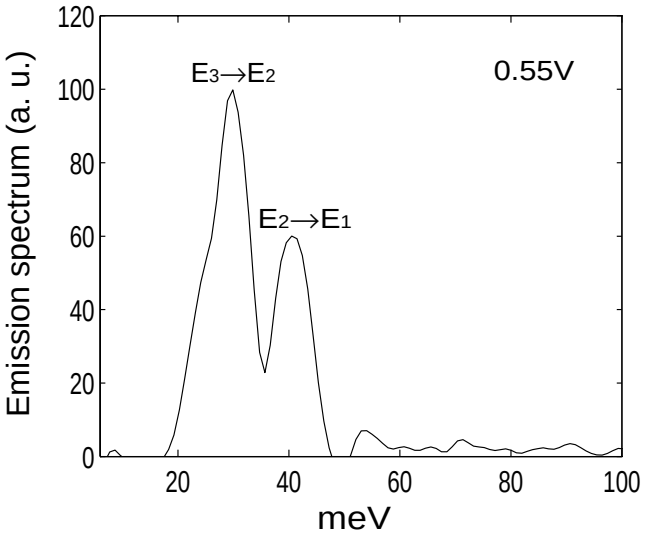

Fig. 8: (Left) Far-infrared measurement set-up that uses an external Fourier transform spectrometer to spectrally resolve the emitted THz signals.

Mid-Infrared Quantum-Cascade Lasers

Personnel

B. Williams and B. Riely
(Q. Hu, in collaboration with Professor M. R. Melloch - Purdue University)

Sponsorship

Army Research Laboratory Federated Lab.

High-power, compact mid-infrared (8 - 12 μm) lasers are very useful tools for remote sensing, end-point detection in dry etching processes, point-to-point communication, and night vision applications. Conventional laser diodes operating in this long wavelength range use narrow-gap lead-salt semiconductors, which require cryogenic operations, provide relatively low power levels, and have very limited frequency tunability. Recently developed Quantum-Cascade (QC) lasers based on intersubband transitions have shown much higher operating temperatures and a great frequency tunability. These features make them ideal for the above-mentioned applications. In this project, we are developing mid-infrared quantum-cascade lasers based on GaAs/AlGaAs quantum-well structures. Compared to the InGaAs/InAlAs materials used in the original quantum-cascade lasers developed at Bell Labs, the GaAs/AlGaAs system offers a much higher thermal conductivity (approximately a factor of 20 compared to InGaAs/InAlAs) and therefore a higher-power operation.

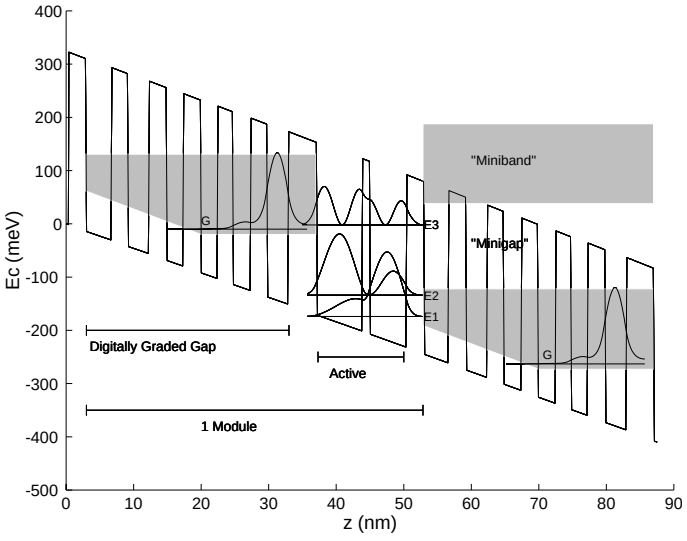

Fig. 9: Conduction-band profile and wave functions of the designed MQW structure that contains a three-level gain medium and superlattices for selective injection and removal of electrons.

The core of our MQW structure is a tightly coupled double quantum well, in which three energy levels form the three-level lasing structure. These energy levels are shown in Figure 9. The lasing transition is to take place between E_3 and E_2, with the energy separation approximately 120 meV, corresponding to 10-μm wavelength. The energy separation between E_2 and E_1 is designed to be approximately 36 meV, which is the energy of LO phonon in GaAs. Consequently, the energy level E_2 will be depopulated by very fast LO-phonon scattering (~0.2 ps). Our design of the MQW structures is aided by a numerical code that solves Shrödinger and Poisson equations self-consistently, and it includes the effect of band nonparabolicity to account for the much higher energy levels corresponding to infrared frequencies.

The superlattice structure sandwiching the active region serves the purpose of selective injection of electrons into the E_3 level, and selective removal of electrons from both E_2 and E_1 levels. By choosing the period of the superlattice properly, the Bragg reflection results in minigaps (transport forbidden) and minibands (transport allowed), as shown in both Figures 9 and 10. The combination of the selective injection into E_3 and the fast removal from E_2 will assure an inverted population between these two levels. We calculated the dipole moment for the $E_3 \rightarrow E_2$ transition to be approximately 23 Å, which yields a modal gain of 480 cm^{-1} for a doping concentration of $1.5 \times 10^{11}/cm^2$. Such a high level of gain is characteristic of the QC lasers in which the two subbands track each other in momentum, resulting in a large joint density of states.

continued

continued

We have fabricated a MQW structure consisting 40 nominally identical structures as shown in Figure 9. An emission spectrum with the narrowest linewidth is shown in Figure 11. The center frequency of 121 meV (corresponding to 10-μm wavelength) is what we designed for, and the FWHM linewidth is only 10.8 meV. This linewidth is comparable to the narrowest achieved at Bell Labs using InGaAs/InAlAs structures, and is an indication of the high interface quality and uniformity of our MQW structures. Currently, we are designing suitable cladding layers for mode confinement to achieve lasing. ❑

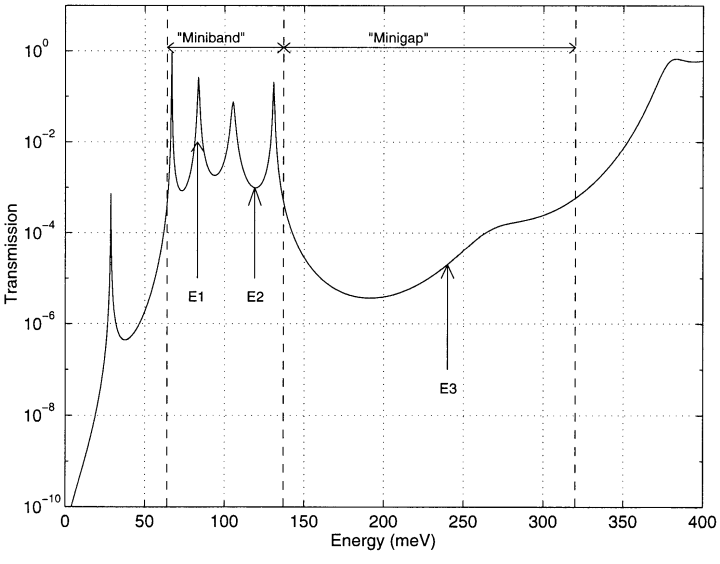

Fig. 10: Calculated transmission coefficient of the superlattice sandwiching the core structure. The valley in the transmission corresponds to the minigap and the peaks form the miniband.

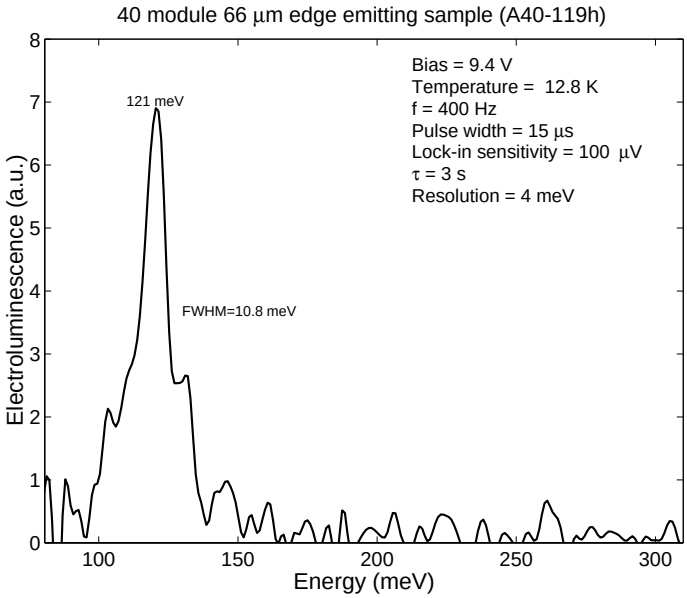

Fig. 11: Spectrum of spontaneous intersubband emission from a 40-module MQW structure whose design is shown in Figure 9.

Optically Pumped THz Emitters using Quantum Wells

Personnel

I. Lyubomirsky
(Q. Hu in collaboration with Professor M. R. Melloch - Purdue University)

Sponsorship

AASERT through US ARO and the Hertz Foundation Fellowship

Compared to electrical pumping, optical pumping offers advantages of an easier design, a higher selectivity in pumping, and a separation of the pump and electrical bias. For THz emitters, easily available CO_2 lasers can be used as the pumping source. We first designed a three-level system for THz emission. However, this structure showed an excessive heating when it is pumped by an intense CO_2 laser. In order to increase the emission efficiency and therefore the gain of the active medium, we have redesigned our optically pumped THz emitters based on a four-level system using coupled triple quantum wells, as shown in Figure 12. Electrons on the ground state E_1 can be pumped by a CO_2 laser to the E_4 level. By carefully engineering the scattering rates between subband levels by choosing subband energy separations and spatial locations, a population inversion between E_3 and E_2 can be achieved. It was estimated that a modal gain of approximately 100 cm^{-1} can be achieved at a 1-W average pump power level. ❑

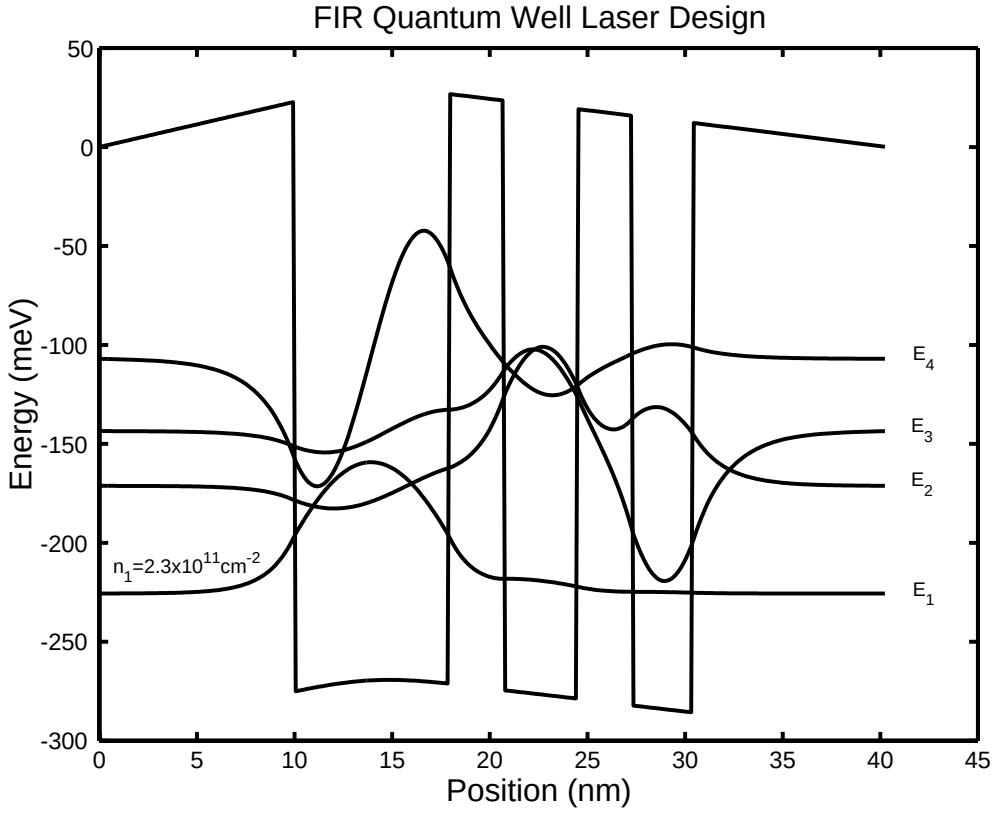

Fig. 12: Schematic of a four-level system based on a coupled triple quantum-well structure. Electrons can be pumped from the E_1 to the E_4 level by a CO_2 laser. They then quickly relax to the E_3 level by LO-phonon scattering. Similarly, the electrons on the E_2 level can be emptied quickly to E_1 through LO-phonon scattering. THz emission is to take place between E_3 and E_2.

Coupled Rings of Josephson Junctions: Interactions of Topological Kinks

Personnel

A. E. Duwel, P. Heij, and E. Trías
(T. P. Orlando, P. Heij-Delft University of Technology, Dr. H. S. J. van der Zant-Delft University of Technology, and Prof. S. Strogatz-Cornell University)

Sponsorship

NSF Grant

We explore a system of two discrete rings of underdamped oscillators, using inductively coupled Josephson junctions as an experimental realization. This Josephson system is a model system for studying spatiotemporal dynamics of coupled oscillators, and more specifically for exploring kink interactions in discrete lattices, a topic that is also important in, e.g., the dynamics of dislocations and ferromagnetic domain walls.

The layout of a discrete coupled ring system with N junctions per ring is shown in Figure 13 for $N = 4$. The Nb-AlO_xNb junctions are 3 x 3 μm^2, and the radius of the outer ring is 28 μm. When the system is cooled in the presence of a perpendicular magnetic field to below the superconducting transition, the total flux bounded by the continuous superconducting rings becomes trapped in units of $\phi_o = h/2e$. A single unit of quantized flux is called a vortex if the flux is along the applied field and an anti-vortex if it is opposite. A vortex and anti-vortex correspond to a kink and anti-kink. If there are $m_{v,in}$ and $m_{v,out}$ kinks in the two rings, and $m_{a,in}$ and $m_{a,out}$ anti-kinks, then the net, conserved phase winding in each ring is $M_{in} = m_{v,in} - m_{a,in}$ and $M_{out} = m_{v,out} - m_{a,out}$. In Figure 13 we show a simulated IV characteristic for the case of $M_{in} = 1$ and $M_{out} = 0$. There are $N = 51$ junctions in each ring. For a range of bias currents ($I_b < 0.57\ I_c$), kink/anti-kink pairs are excited in the outer ring. In the figure, we use an open circle to represent kinks and a cross to represent the anti-kink. The inset shows the relative motions of the kinks and the anti-kink when one pair is excited in the outer ring. As the bias current is applied, the kinks and anti-kink begin to rotate, producing a dc voltage across each ring.

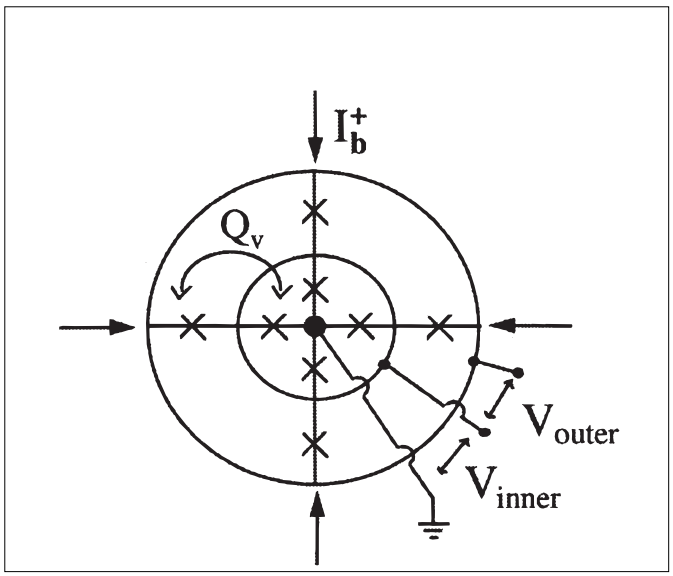

Fig. 13: Schematic of inductively coupled ring system. A uniform current I_b is fed into each node, as indicated by arrows and is extracted from the enter island. In experiment, we measure the dc voltages V_{inner} and V_{outer}. Q_v is the mutual inductance between two adjacent cells of the inner and outer rings.

In Figure 14, we plot the average dc voltage for each ring vs. bias current. As the current is increased, the kinks move faster, and the dc voltage increases. The kinks and anti-kinks phase-lock with linear waves, and, at certain speeds, further increases in the bias current tend to increase the amplitudes of the excited linear waves rather than the speed of a kink. As a result, at a step of almost constant voltage appears in the IV. These special speeds are given by the dispersion relation for linear waves in the coupled system, which is split into two branches. We refer to the inner ring step at $0.0151\ I_cR_n$ as an Eck step, since the single trapped kink is near its maximum speed and no additional pairs are excited. When pairs are excited, their contributions simply add up (to lowest order), resulting in voltage steps at much larger voltages. We refer to these as High-Voltage (HV)

continued

steps, since they are similar to states that can exist on the return path of an isolated ring. A study of the particular dynamics on these steps reveals that the coupling between the rings gives rise to phase-locking between kinks of the same sign in different rings. The kinks in both rings travel together at the same speeds. The anti-kinks travel in an opposite direction and can even have speeds that are different from the kinks.

In experiments of N = 4 and N = 8 systems, we discovered another interaction effect. For every distinct combination of M_{in} and M_{out}, we observe a parameter regime where pairs are excited only in the outer ring, another parameter regime where pairs are excited only in the inner ring, and a transition region in temperature from one state to the other. In addition, in several experiments we observe a very narrow range of temperature where there is a time-dependent competition between the two states. Based on the time scales of the fluctuations, the dynamics are likely to be influenced by weak noise in the input parameters. However, the sudden vulnerability of the system at this particular point also implies the presence of an instability and the possibility of a novel dynamical state. Future experiments will address the role of noise in this two-state competition. ❑

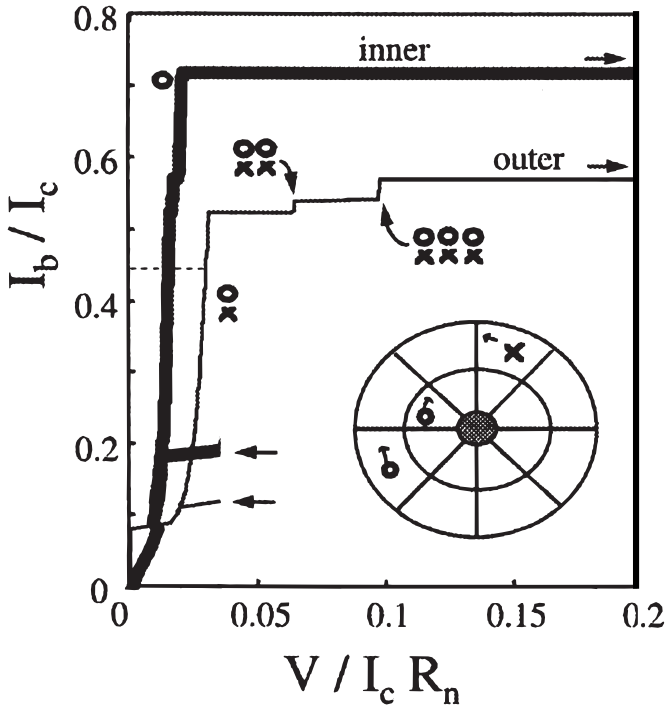

Fig. 14: Simulated IV characteristic. The nearly constant voltage steps correspond to the motion of the kinks (represented by open circles) and anti-kinks (represented by crosses) at their maximum speeds. The inset shows the relative motion of the kinks and the anti-kink for one excited pair in the outer ring.

Engineering Josephson Oscillators

Personnel

E. Trías and A. E. Duwel
(T. P. Orlando, Dr. S. Watanabe-University of Minnesota, and Prof. S. Strogatz-Cornell University)

Sponsorship

NSF Grant

As the telecommunications revolution pushes for denser utilization of the spectrum, there is a need to develop inexpensive sources and detectors that operate in the 100 GHz to several THz range. It is precisely in this range that Josephson junctions provide an almost ideal solid state, current controllable source.

Arrays of junctions provide for relatively large power but due to non-linearities they can exhibit diverse complex spatiotemporal patterns. Experiments, simulations and analysis were performed on a broad range of discrete arrays of Josephson-junction oscillators in order to understand their ability to produce coherent radiation. Networks ranging from single square and triangular plaquettes to one- and two-dimensional arrays are studied. In each array, the junctions are identical and underdamped, and the arrays are driven by dc bias currents. Although few analytical results are known for these systems, we study the technically interesting solutions, which can be represented as traveling waves. It is in this mode that the devices can be used as submillimeter wave sources.

Using the mathematical technique of harmonic balance it is possible to create an equivalent linear circuit of a Josephson network that is operating in a traveling wave mode. Though the non-linearity of the system allows for mixing of all the harmonics, in underdamped systems we find that the first harmonic is orders of magnitude stronger than the rest. In general any variable can be decomposed in terms of its dc and ac spectrum. If we further restrict the ac component to a single frequency as suggested by our simulations, then the branch current and voltage across a junction can be written as

$$I = I_{DC} + i_{ac} e^{j\omega t}$$
$$V = V_{DC} + v_{ac} e^{j\omega t}$$

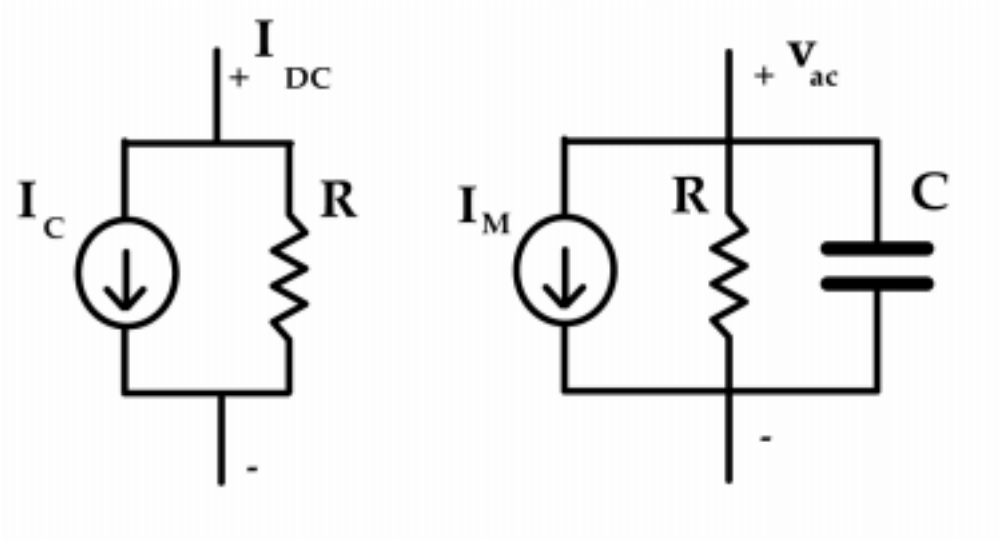

Fig. 15: Equivalent circuit for a Josephson junction in a voltage state and with a single harmonic. Non-linearity is captured by I_M, which is a mixing current that describes the interaction between the rotating Josephson phase and its first harmonic.

continued

Our equivalent circuit then consists of a dc bias circuit and a mixing circuit that creates the first harmonic. Figure 15 depicts the equivalent circuit. Here k represents the phase difference between the first harmonic and the rotating part of the Josephson oscillation, and the mixing current, I_M, represents the nonlinear interaction between them. This equivalent circuit makes it possible to use powerful circuit theoretic tools to understand a Josephson network.

A natural application of the circuit model is the study of the effect that the boundaries have on the traveling wave. Figure 16 shows the spatial distribution of first harmonic amplitudes in a parallel Josephson array of 54 junctions. The graph (a) shows the array with open boundaries. In general the shape will depend on the array parameters, but at this value of applied field the spatial part of the solution is symmetric. The reflection of the traveling wave is clearly evident on both the entry and exit sides of the array. Using the above circuit model it is possible to determine a load impedance that will minimize the reflection. Graph (b) shows the result when the impedance matching load is applied to junction one. The reflection at the left-hand boundary is reduced substantially.

We plan to use the linear circuit model to understand how to optimize a Josephson oscillator design so that a minimum of linewidth is obtained while providing a maximum of power and frequency tunability. ❑

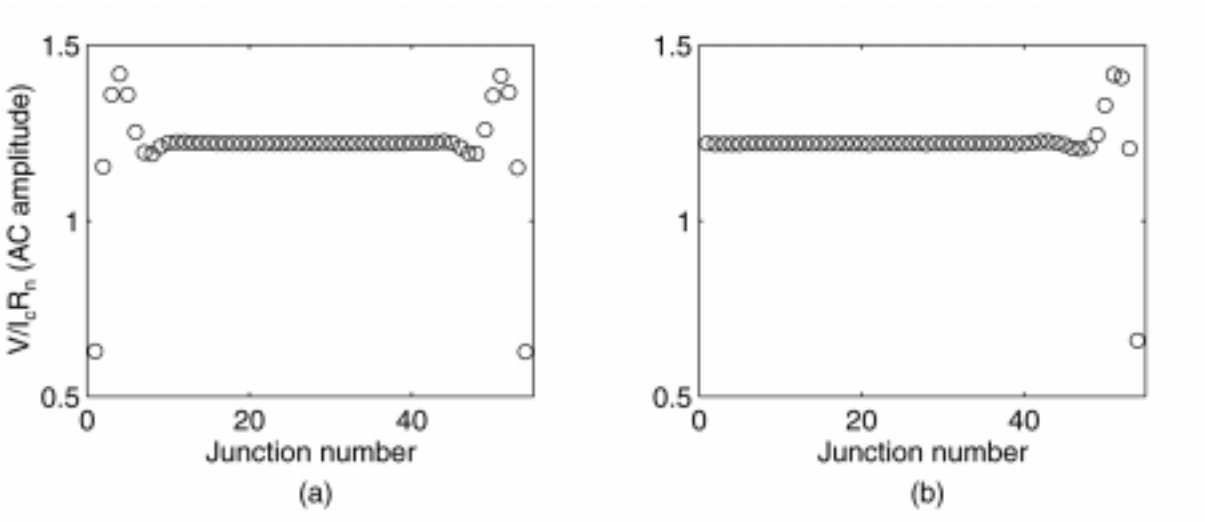

Fig. 16: Amplitudes of first harmonics of vertical junctions in a parallel array. Graph (a) is an array with open boundaries while (b) shows the same array with a matching load at junction one.

Meissner-like States in Josephson Arrays

Personnel

E. Trías and J. Jensen
(T. P. Orlando)

Sponsorship

NSF Grant

One of the most striking features of superconducting materials is their ability to expel an applied flux. This perfect diamagnetism is direct expression of macroscopic quantum mechanical effects and is usually called the Meissner effect. A Meissner state occurs when the induced flux caused by persistent currents in the superconducting material almost perfectly cancels the applied flux.

In order to study this effect in Josephson networks, we designed several ladder arrays with different number of rows. The arrays consist of square loops with junctions on both vertical and horizontal edges. As we increase the applied current from zero, the array is superconducting and therefore has zero output voltage. At some critical current the array develops a finite voltage and the zero voltage state is destroyed. It is in this zero voltage state that the Meissner state can exist.

To measure the critical current of an array, we first apply a perpendicular magnetic field, H_A. Once the field is set, the current is swept from zero until the output voltage reaches a threshold value that is typically set to 1 μV. Figure 17 shows representative I_{dep} vs. applied field curves for four different arrays: 47 x 47, 3 x 47, 2 x 47, and 1x15. The 47 and 15 refer to the number cells in the direction normal to current injection while the smaller number is the number of rows in the direction of the applied current.

We find generic features for all the measurements regardless of temperature or array topology. First, the shape of the I_{dep} curves is periodic with the applied field. We normalize the applied field so that $f = H_A/H_{period}$ and the curves become periodic with $f = 1$. Secondly, the curves are almost symmetric about $f = 0.5$. The details of the I_{dep} vs. f curves are sample dependent as shown in Figure 17. For the 47 x 47 ladder, we find that a large narrow peak is observed at $f = 0$. As f is increased the curve quickly decays to an average level of 0.17. There are smaller peaks that are evident at $f = 1/4$, $f = 1/3$ and $f = 1/2$. The 3 x 47 array has a similar feature to the fully

Fig. 17: I_{dep} vs. frustration for four different arrays: 47 x 47, 3 x 47, 2 x 47, and 1 x 15. The 47 and 15 refers to the number cells in the direction normal to current injection while the smaller number is the number of rows in the direction of the applied current. Lines with arrows indicate broadening of $f = 0$ peak as the number of rows of the array decreases.

continued

two-dimensional system. The peak at $f = 0$ is now broader as marked by the arrow. The decay to the average level is linear but the substructure appears at different f values. When the array only has two rows we see curves typical to the 2 x 47 ladder. The $f = 0$ peak is now very broad, but the decay is still linear. All of the other structure has disappeared except for the $f = 0.5$ peak. Finally, when we measure an array with only one row, the $f = 0$ peak has expanded so that even the $f = 0.5$ substructure has disappeared. It is this peak at $f = 0$ that can be described as a Meissner-like state.

After performing numerical simulations to characterize the Josephson network dynamics, we have developed a model that reproduces the experimental characteristics. We find that even if the geometrical inductances are neglected, the Josephson junctions that circumvent the network can act as parametric inductors that support a circulating current. As the network becomes more two-dimensional it becomes increasingly difficult to support the large circulating current and so the Meissner-like state narrows. The linear decay can be described in terms of Ampère's law. However, it is still not fully understood how the state is destroyed or what the substructure that is so evident in Figure 17 represents. We will continue to investigate these and other unsolved problems. ❑

Self Field Effects on Flux Flow in Josephson Arrays

Personnel

E. Trías
(H. S. J. van der Zant-Delft University of Technology and
T. P. Orlando)

Sponsorship

NSF Grant

Two-dimensional arrays of Josephson junctions provide controllable model systems for the study of vortex transport in thin film superconductors. A crucial parameter that determines the dynamics of these vortices is the characteristic penetration depth of the applied field. It is this length that also governs the effects of self-induced magnetic fields.

Typical current-voltage *IV* characteristics vs. applied magnetic field are shown in Figure 18. The applied magnetic field B_0 is measured in units of the frustration $f = B_0 p^2/\phi_0$. The depinning current I_{dep} indicates the onset of the flux-flow region. There is a curving transition in the *IV* from the depinning current to a linear region. The flux-flow resistance R_{ff} is defined as the slope of this linear region, which is shown by a straight line for each of the *IV*s. The inset shows that the assigned resistance values are linear in *f* up to $f \approx 0.3$. For larger values of *f* up to $f = 0.5$, R_{ff} is no longer linear with *f* due to the increased interaction between vortices.

Other measurements and numerical studies of the effects of self-induced magnetic fields on the flux flow resistance have been performed. It was found that the flux-flow resistance becomes larger as the penetration depth of the array decreases. A phenomenological model, which agrees qualitatively with the experiments and simulations, has been developed to explain the self-field effects on flux flow. Due to the smaller spatial extent of supercurrents around a vortex when self-fields are important, both the mass of the vortex and the array viscosity decrease. The decreased mass and viscosity lead to an increase in flux-flow resistance. The effects of spin-wave damping have also been investigated for underdamped arrays.

The flux-flow region appears to be richer in its dynamics than the presented model can account for. In particular, treating the effective linear viscosity of the array as the sum of the Bardeen-Stephen damping and spin-wave damping is probably an over-simplification. Though these deviations do not diminish the useful and intuitive results from the phenomenological model, they do point the way for further research on the richness of the dynamics in the flux-flow regime. ❑

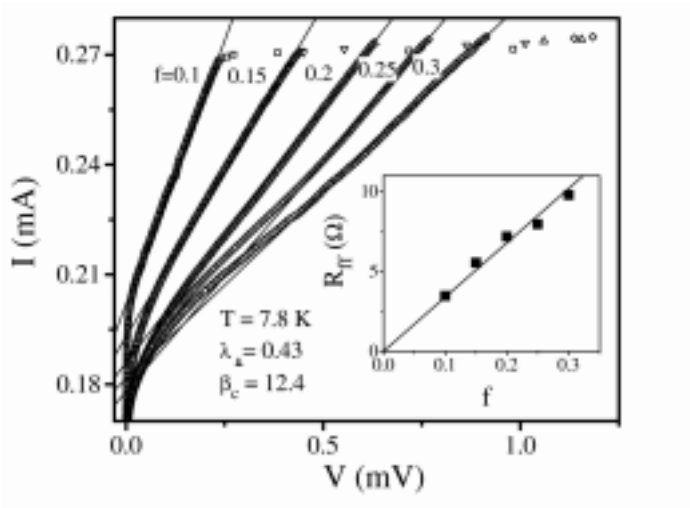

Fig. 18: Current-voltage characteristics for various magnetic fields from f = 0.1 to 0.3. The was taken at 8.6K with $\lambda_\perp = 1.04$ and $\beta_c = 5.1$. The numbers indicate values of f. The solid straight lines denote the linear region of flux-flow. The inset shows that the flux-flow resistance R_{ff} is linear in f.

Nonlinear Dynamics of Discrete Josephson Arrays

Personnel

E. Trías and A. E. Duwel
(M. Barahona-Stanford University, T. P. Orlando, Dr. H. S. J. van der Zant-Delft University of Technology, Dr. S. Watanabe-University of Minnesota, and Prof. S. Strogatz-Cornell University)

Sponsorship

NSF Grant

Discrete arrays of nonlinear Josephson oscillators can exhibit diverse spatiotemporal patterns. Although such oscillator arrays are difficult to analyze completely, one can often use the symmetries of the system to construct simple patterns composed of spatially repeated "unit cells". Experiments, simulations, and analysis on a broad class of discrete arrays of Josephson-junction oscillators indicate novel phase-locked states that due to their special symmetry reduce the governing equations of the full array to a much smaller set of equations of a unit cell. Networks ranging from single square and triangular plaquettes to one- and two-dimensional arrays have been studied.

Figure 19 shows the measured *IV* curves (*I* is the current per vertical junction normalized by I_c and *V* is the voltage per row) for three different array geometries when fully frustrated. The signature of all these *IV*'s is the appearance of jumps at two resonant voltages, V_+ and V_-. The upper step, which ends at V_+ is independent of temperature suggesting that local geometrical properties determine the voltage. In this state, all the rows of the array act coherently and phase-lock at a voltage that depends on the geometric loop inductance and junction capacitance. The lower voltage V_-, on the other hand, is temperature-dependent, suggesting a dependence on the Josephson inductance and the geometric loop inductance. By taking advantage of the symmetry of the network it is possible to describe the solution as a dynamical checkerboard state and mathematically analyze its resonant behavior in a reduced system of governing equations. However, the conditions for the stability and the temporal periodicity of the checkerboard state and the dynamics associated with other possible states, are challenging problems for future investigation.

We have also studied the spatiotemporal dynamics of circular one-dimensional arrays of underdamped Josephson junctions connected in parallel. In these Josephson rings, a traveling wave solution consisting of a single kink can be trapped and studied experimentally without the complications caused by reflections off boundaries. We find that a propagating kink can become phase-locked to linear waves excited in its wake. In the *IV* curve, resonant steps are observed indicative of this phase-locking. Resonant steps also occur in the *IV* curves for higher voltages in the return path of the subgap region. These resonant steps have a completely different origin and occur at voltages where the periodic whirling solution undergoes an instability parametrically amplified by the linear modes in the system. ❑

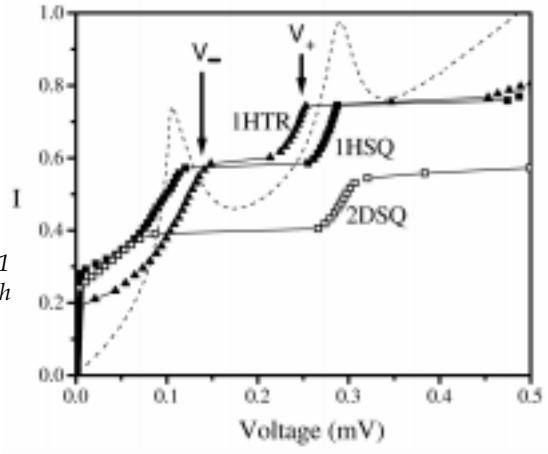

Fig. 19: Experimental IV curves for three arrays: triangular array (1 X 9 Plaquettes) with $\beta_c = 8$ and $\lambda\perp = 0.64$; square array (1 X 7) with $\beta_c = 11$ and $\lambda\perp = 0.76$; and a square array (7 X 7) with $\beta_c = 20$ and $\lambda\perp = 0.92$. Dashed line, IV from harmonic balance for the square array (1 X 7) array with the same β_c and an effective $\lambda\perp_{eff} = 0.61$ which accounts for mutual inductance effects. V_+ and V_- are indicated.

Triangular Arrays of Josephson Junctions

Personnel

A. E. Duwel
(P. Caputo-KFA - Julich, GE, A. Ustinov-Universität Erlangen-Nüremberg, GE, S. Yukon - Rome Laboratory, N. C. H. Lin - Rome Laboratory, and T. P. Orlando)

Sponsorship

AFOSR and Rome Laboratory

Triangular arrays of Josephson junctions operating in an applied magnetic field have been proposed as a way of obtaining useful power levels of mm and sub-mm wave radiation generated by the AC Josephson effect. A triangular one-dimensional (1D) array consists of a single row of parallel biased triangular cells, which have a Josephson junction in each branch (Figure 20). The bias current is uniformly applied through resistors at each point indicated by arrows in the sketch, and the array voltage response is read across the row. In order to characterize high frequency properties, the horizontal junctions of the array (x-direction) are integrated in an insulating SiO_2 layer of a superconducting microstripline ending with a finline antenna. The antenna transforms the array impedance into the waveguide impedance through two exponentially tapered Nb fins.

.

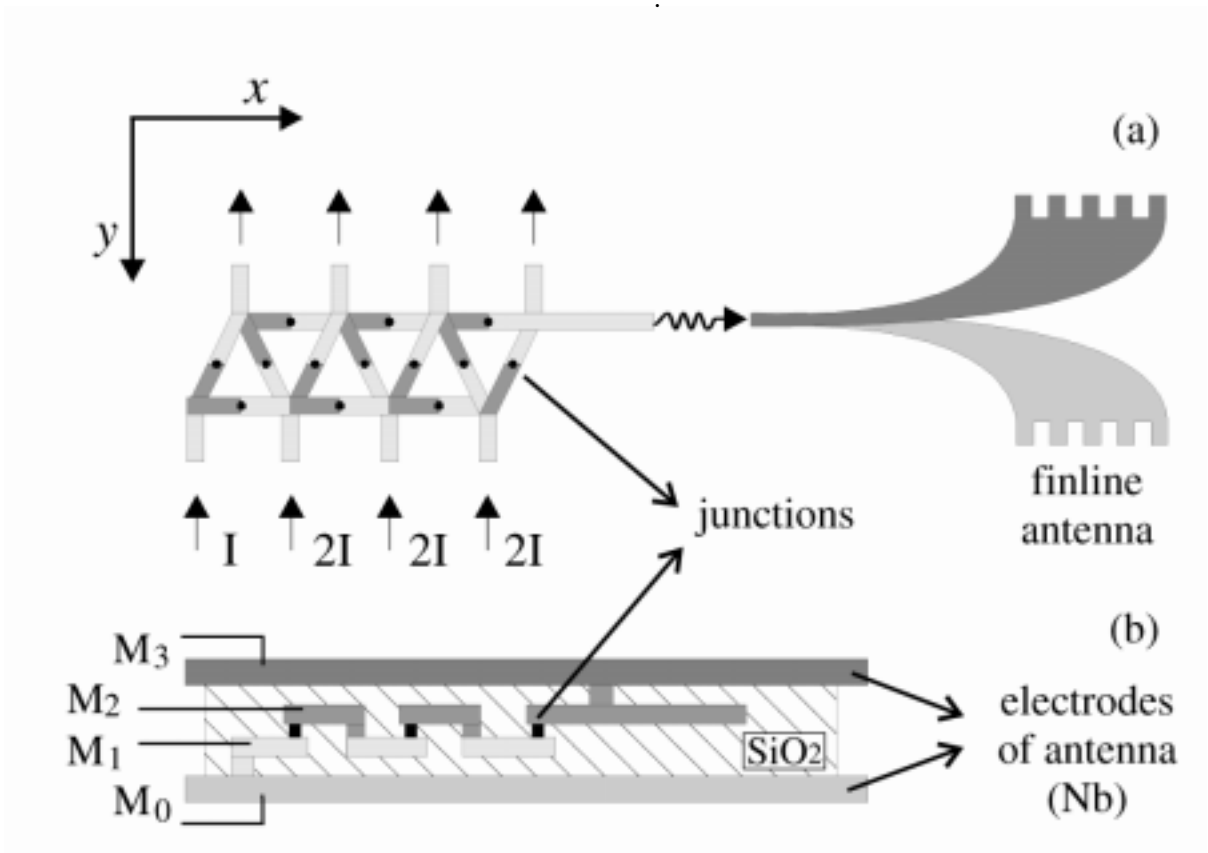

Fig. 20: Schematic top view of a 6 cell triangular array with the finline antenna which couples the array signal to the 80 - 120 GHz rectangular waveguide (a) and a cross view of the horizontal junctions of the array inserted in the microstripline ending into the antenna (b).

continued

In the presence of a field, two resonances appear on the IV curve, corresponding to L_SC and L_JC resonances. These steps are characteristics of single cells, and their voltage does not change with the number of cells in the array. At the L_SC resonance, triangular arrays produce large-amplitude single-harmonic oscillations in the horizontal junctions. High frequency measurements of a 12 cell triangular array reveal the presence of radiation emitted from the transverse junctions. Figure 21 shows the radiated power PRAD at 75 GHz, detected at the L_SC step. The radiation frequency is proportional to the step voltage. Measurements of longer rows will be taken to test the scaling of power with the number of horizontal junctions. ❑

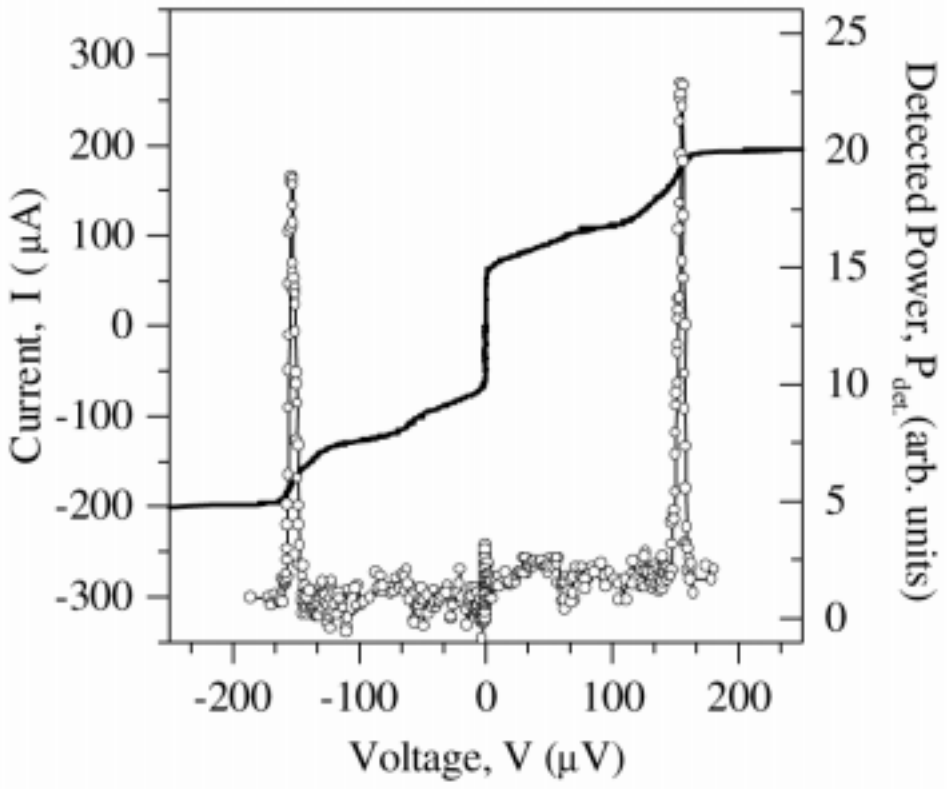

Fig.21: Measurement of radiation emission from a 12-cell array. The IV curve is shown together with the detected radiation power at a frequency v = 75 GHz. The detector bandwidth is Δv = 0.9 GHz.